



# Photonic-enabled beam steering at 300 GHz using a photodiode-based antenna array and a polymer-based optical phased array

SIMON NELLEN,<sup>1,\*</sup> TIANWEN QIAN,<sup>1</sup> GARRIT SCHWANKE,<sup>1</sup> SEBASTIAN LAUCK,<sup>1</sup> DAVID DE FELIPE,<sup>1</sup> MORITZ KLEINERT,<sup>1</sup> MILAN DEUMER,<sup>1</sup> LARS LIEBERMEISTER,<sup>1</sup> MORITZ BAIER,<sup>1</sup> BJOERN GLOBISCH,<sup>1</sup> NORBERT KEIL,<sup>1</sup> ROBERT B. KOHLHAAS,<sup>1</sup> AND MARTIN SCHELL<sup>1,2</sup>

<sup>1</sup>Fraunhofer Institute for Telecommunications, Heinrich Hertz Institute, Einsteinufer 37, 10587 Berlin, Germany

<sup>2</sup>Technische Universität Berlin, Institut für Festkörperphysik, Hardenbergstraße 36, 10623 Berlin, Germany  
[simon.nellen@hhi.fraunhofer.de](mailto:simon.nellen@hhi.fraunhofer.de)

**Abstract:** For wireless networks beyond 5G, directivity and reconfigurability of antennas are highly relevant. Therefore, we propose a linear antenna array based on photodiodes operating at 300 GHz, and an optical phased array based on polymer waveguides to orchestrate the antennas. Due to its low thermal conductivity and high thermo-optical coefficient, the polymer chip enables highly efficient and crosstalk-free phase shifting. With these, we demonstrate purely photonic-controlled beam steering across 20°. Compared to a single emitter, the 3-dB beam width is reduced by 8.5° to 22.5° and the output power is >10 dB higher. Employing Snell's law for coupling into air, we can precisely predict the radiation patterns.

© 2022 Optica Publishing Group under the terms of the [Optica Open Access Publishing Agreement](#)

## 1. Introduction

Continuous-wave terahertz technology based on optoelectronic conversion is well-established as a spectroscopic tool due to its large bandwidth ranging from below 100 GHz up to 4.5 THz and a resolution below 7 MHz [1–3]. This approach also enables measurement rates up to 200 spectra per second [4]. Beyond science labs, these systems are also suitable for sensing applications in industrial environments, such as non-destructive testing [4,5]. Due to the increasing demand for higher data rates and bandwidth in wireless communications, carrier frequencies in the (sub-)terahertz range are already standardized for 5G and beyond 5G (B5G) [6]. Because of atmospheric absorption, many research activities aim for wireless links around 300 GHz [7–10]. At such high carrier frequencies, channel bandwidths above 50 GHz are feasible for radio communications [6,9,11]. Photonic generation of terahertz waves is directly compatible with optical fiber communication technology allowing to create such high-bandwidth channels. In addition, the photonic approach benefits from mature devices developed for optical fiber communications: high-speed photodiodes to convert an optical beat signal into an electrical signal in the terahertz range, lasers generating the optical beat signal, and modulators to imprint the data onto the signal in the optical domain. Using photonic technology, high-capacity wireless links have already been demonstrated [12–22].

In previous studies, we investigated the radiation pattern of antenna-integrated PIN photodiode modules, and their capability as transmitters in 300 GHz links [16,18,23,24]. However, single element photonic emitters suffer from two fundamental limitations: the emitted power is limited due to saturation of the photodiode, and the antenna directivity is limited due to the finite effective aperture of the planar antenna. For communication applications, this results in limited signal-to-noise ratio at the receiver, i.e., limited data rate and limited link distance. Antenna arrays

are an established approach to overcome these limitations. In addition, antenna arrays enable beam steering, i.e., changing the beam angle without mechanical movement of the transmitter, only by setting the phase of the single antenna elements [25,26]. In order to achieve all these improvements compared to a single element antenna, the distance between the antennas of the array needs to be less than the radiated wavelength  $\lambda$ . Thus, photonic integration is the key enabler for such phased arrays at terahertz frequencies. Photodiode-based antenna arrays have been demonstrated to be suitable for terahertz beam steering [27,28]. To avoid free-space optical delay lines, integrated optical phased arrays (OPAs) based on silica waveguides have been demonstrated to control such an antenna array [29].

In this work, we present a phased antenna array with broadband bowtie antennas, which are suitable to cover multiple frequency bands from millimeter waves to terahertz frequencies. We employ photonic integration techniques to combine four PIN photodiodes with integrated antennas on a single indium phosphide (InP) chip. On-chip optical amplifiers are integrated to reduce the required optical input power. In addition, we developed an optical phased array based on HHI's polymer-based hybrid integration platform PolyBoard. This is the first demonstration of a polymer-based OPA. The polymer material offers a high thermo-optical coefficient and low thermal conductivity, which allows crosstalk-free phase control. Optical interfaces are designed for coupling to InP waveguides and optical fibers, which enables pigtailed or hybrid integrated devices. Employing the OPA in combination with the antenna array as a 300 GHz emitter, the 3-dB beam width is reduced by 27% from  $31^\circ$  to  $22.5^\circ$  and we demonstrate 1-dimensional beam steering across  $20^\circ$ . In contrast to previous published work, waveguide technology of the InP and polymer platform are compatible [27–29]. Thus, the OPA array and antenna array can potentially be assembled into a hybrid photonic integrated circuit for broadband terahertz generation including beam steering [30,31].

## 2. Design of a phased terahertz antenna

In order to direct the radiated signal of the emitter to the receiver in the application scenario for communication or sensing, the beam angle of the terahertz transmitter needs to be adjustable. In the case of coherent radiation through an antenna array, this can be achieved by a phase difference of the individual antennas, i.e., a phased array.

For a phased antenna array, the beam angle  $\theta^\circ$  is defined as the angle between the center of the main lobe and the axis of the array elements [25,32]. For the theoretical prediction of the beam angle  $\theta^\circ$ , the following parameters of the phased array need to be specified: the spacing of the individual antenna elements  $d$ , the phase difference of the individual antennas  $\beta$  and the wavelength  $\lambda$  of the carrier frequency. The relationship between steering angle and properties of the array is then given by [25]

$$\cos(\theta^0) = -\frac{\lambda}{2\pi} \cdot \frac{\beta}{d}. \quad (1)$$

### 2.1. Array factor

The array factor (AF) is the radiation pattern of an antenna array (AA) under the assumption that each single antenna element (AE) of the array radiates isotropically with the same power [25,32]. With the given properties of the antenna array, i.e., number of antenna elements  $N$ , their distance  $d$ , and the wavelength  $\lambda$ , it is possible to predict analytically the angular radiation for a certain phase shift  $\beta$  between the single antenna elements. Therefore, the normalized array factor can be calculated as [25]

$$AF = \frac{1}{N} \left[ \frac{\sin\left(\frac{N}{2}\Psi\right)}{\sin\left(\frac{1}{2}\Psi\right)} \right], \text{ where } \Psi = \frac{2\pi}{\lambda} \cdot d \cdot \cos(\theta) + \beta. \quad (2)$$

Hence, the AF is a function of the radiation angle  $\theta$  indicating the normalized intensity at a certain angle considering the array's properties except for the actually radiation of the single AE. Since anisotropic antennas are used for our antenna array, the individual radiation of the AEs are not isotropic. In this case, the normalized radiation from the antenna array can be predicted by multiplication of the radiation pattern of a single antenna element with the array factor:

$$AA(\beta, \theta) = AF(\beta, \theta) \cdot AE(\theta). \quad (3)$$

AA, AF, and AE describe the angular distribution of the radiation as a function of  $\theta$ . In case of a single antenna element AE, the angular distribution is independent of the phase  $\beta$ .

## 2.2. Impact of antenna and lens

Planar antennas are widely used for terahertz emitters and receivers due to their possibility for monolithic integration. Therefore, the metallic antenna structure is processed next to the photonic or electronic mixer on top of the respective semiconductor substrate [2,23,33–37]. A common way to couple the radiation from the substrate into free-space is attaching plano-convex lenses with a refractive index close to the substrate [38–41]. In addition to the enhanced coupling into free-space, this method also contributes to the beam shaping, e.g. to increase antenna gain, due to the lens properties. However, for an antenna array, the beam shaping feature is counter-productive. Thus, we used a hyper-hemicylindrical silicon lens for the 1-dimensional antenna array, which appears flat in the H-plane of the array, i.e., the beam steering plane, but provides lens properties in the orthogonal plane, i.e., the E-plane.

Figure 1(a) illustrates the radiation into a half space of substrate from the phased array of four equidistant AE with a constant phase difference  $(n - 1)\beta$ , i.e., an infinitely large silicon lens. Here the beam angle  $\theta^\circ$  is given by Eq. (1) with the wavelength inside the silicon  $\lambda = \lambda_{Si}$ . For proper beam steering, the distance  $d$  between the single AEs is chosen to be 250  $\mu\text{m}$ , which fulfills the criterion of  $d < 0.9\lambda_{Si}$  at our target frequency of 300 GHz. The resulting AF inside the half space of silicon is shown for a phase difference of  $\beta = 0^\circ$ ,  $\beta = -45^\circ$ , and  $\beta = +45^\circ$  in Fig. 1(b). With this values, a scan sector, i.e., the total beam steering angle, of  $\Delta\theta = 16.8^\circ$  can be achieved inside the silicon [32]. The 3-dB width of the resulting main lobe is  $15.5^\circ$ . Further, side lobes arise for  $\beta = \pm 45^\circ$ , which reach their  $-3$  dB intensity approx.  $70^\circ$  off the main lobe.

In addition to the general considerations regarding beam steering with phased arrays (s.f. 2.1), the refraction of the terahertz wave at the surface between silicon lens and air contributes to the radiation pattern. As illustrated in Fig. 1(c), the terahertz waves refract towards the lens surface according to Snell's law when they transit from silicon ( $n_{Si} = 3.41$ ) to free-space ( $n_{air} = 1$ ). Figure 1(d) shows the theoretical derived array factor of the afore-mentioned antenna array considering Snell's law. The positive effect of this additional refraction is an increased scan sector of  $\Delta\theta = 60^\circ$  for a phase shift of  $\beta = \pm 45^\circ$ . On the other hand, the refraction results in a broadening of the lobes, i.e., the 3-dB width of main lobe is  $54^\circ$  without phase shift and increases to  $70^\circ$  for a phase shift of  $45^\circ$ . Thus, the directivity of the antenna array suffers due to the transition from silicon to air, whereas the beam steering capability is increased. Note that the effect of total internal reflection inside the silicon limits the steering angle to  $\pm 17.01^\circ$  inside silicon, which corresponds to a phase shift  $\beta = \pm 90.06^\circ$ . Due to this total reflection, the side lobes of the AF insides silicon (Fig. 1(b)) are not transferred to the radiation inside free-space.

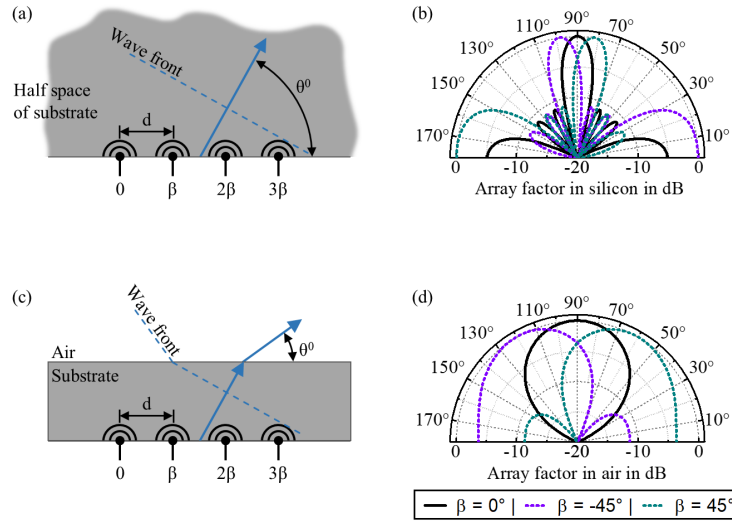


**Fig. 1.** Theoretical radiation from an array of four isotropic antennas with pitch  $d = 250 \mu\text{m}$  at a frequency  $f = 300 \text{ GHz}$  and incremental phase shift  $\beta$ : comparison of radiation assuming an half space of substrate ((a), (b)) and radiation assuming a finite substrate with transition into air ((c), (d)). In (a) the radiation superposes to a common wave front with the beam angle  $\theta^0$ . This array results in an array factor (b), i.e., radiation pattern in the half space, where the beam angle  $\theta^0$  depends on  $\beta$  of the single antennas. With a finite thickness of the substrate (c), i.e., a hyper-hemicylindrical lens, the common wave front experiences a refraction at the transition from substrate to air, which results in an increased beam angle  $\theta^0$ . Taking Snell's law into account for the refraction at the surface, the array factor of this array (d) shows increased beam angles a broadened main lobe.

### 3. Fabricated devices

#### 3.1. Antenna array

Bowtie antennas are well established and characterized in combination with PIN photodiodes for broadband terahertz radiation due to their frequency-independent impedance [2,23,33,41–43]. For this reason, a bowtie structure is also used to realize the antenna array. Contrary to a typical broadband bowtie antenna, this antenna array is matched to the 300 GHz target frequency due to its purpose-matched design: the bowtie has an additional resonance whose frequency is determined by the length of the edge. Compared to conventional dipole antennas, the important advantage of the bowtie antenna is that the angle between the antenna wings can be used to match the feeding point impedance to the source impedance of the diode [44]. An aperture angle of  $110^\circ$  and  $190 \mu\text{m}$  edge length were chosen for matching to the diode at 300 GHz. However, the dimensions of the bowtie limit the minimum distance between individual antennas. In order to reduce the pitch of the antennas, the array is oriented along the H-plane of the bowties.

For our photonic antenna array, we use the generic InP foundry platform at Fraunhofer HHI [45,46]. Figure 2(a) shows the fabricated InP chip with spot size converters (SSC) at the left edge to individually feed the optical signals into the on-chip waveguides. Semiconductor optical amplifiers (SOAs) boost the beat signals before they reach the photodiodes (PDs). The PDs are located in the center of the metallic bowtie wings, which appear grey-violet in the micrograph due to an insulating layer on top. SOAs and PDs are biased via gold-plated lines, which allow for contacting from the edge of the chip. Note that there is an unfortunate mismatch between our first SOA layout and the epitaxial stack of the SOA, which leads to less optical gain than

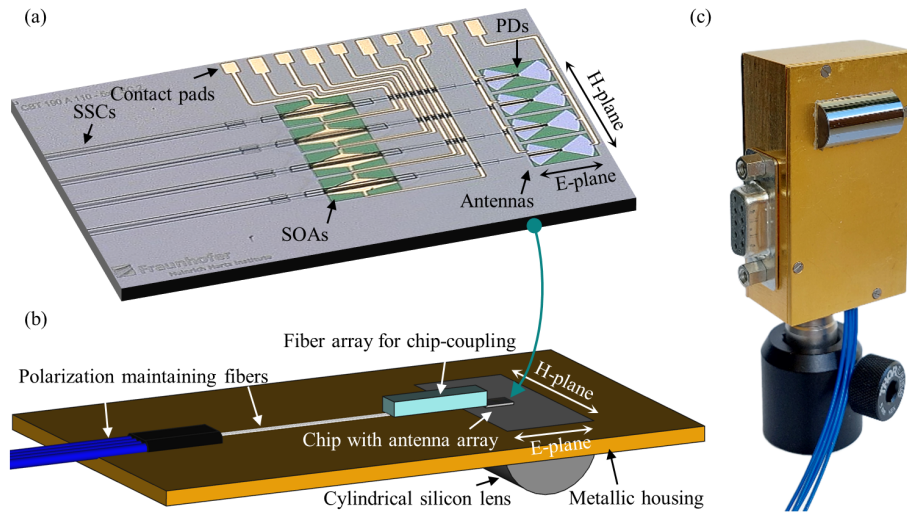


**Fig. 2.** (a) The fabricated InP chip is 2 mm x 3 mm in size. At the left edge, spot-size converters (SSCs) ensure that the mode-field diameter of the optical waveguides on the chip is matched to the optical fiber. Four semiconductor optical amplifier (SOAs) boost the optical signal before the photodiodes (PDs), which feed the antennas with RF current. The contacts for applying the SOA current and biasing the diodes are placed on the top edge of the chip for a compact electrical interface. (b) The CAD model illustrates the packaging of the antenna array: the silicon lens is fixated in the metallic frame to carry the InP chip and the fiber array, which is actively aligned with the SSCs. (c) The final emitter module is a closed package to ensure robustness during field tests. A multi-pin connector enables electrical driving of the SOAs and PDs.

expected. For future SOA-integrated antenna chips, the layout can be easily adapted to ensure a SOA gain between 10 dB and 13 dB, what will be sufficient to compensate the insertion loss of the OPA and provide appropriate optical power the PDs. However, thanks to the possibility of fiber-coupling of our photonic chips, additional optical amplifiers can be added to demonstrate beam steering with the fabricated antenna array. The SOAs with limited gain are used to fine-tune the photocurrent of the PDs.

In order to ensure directivity and avoid side lobes, the distance between the individual antennas of the arrays should be below the target wavelength  $\lambda$ . Due to the use of a silicon lens underneath the antenna chip, we chose an antenna spacing of 250  $\mu\text{m}$ , which corresponds to  $0.86 \cdot \lambda_{Si}$  at 300 GHz. The fabricated bowtie array is mounted on the hyper-hemicylindrical silicon lens with the axis of the cylinder parallel to the antenna array. Since the bowtie antennas are lined up along the H-plane, the lens only shapes the radiation in the E-plane.

Figure 2(b) shows the 3D model of the emitter module including the InP chip, silicon lens, and optical fiber array. The latter allows to feed the four optical input signals from the OPA parallel into spot size converters on the InP chip, which are only separated by 250  $\mu\text{m}$  and, thus, cannot be coupled by individual fibers. The fiber array is aligned actively, i.e., while monitoring the photocurrent of the PDs, in front of the antenna chip and then fixated to the metal carrier, which later is the front plate of the housing. Figure 2(c) shows a picture of the packaged module. In order to assure stable and robust electronic connection during the operation in the beam steering testbed, bias voltage for the photodiodes (PDs) and supply current for the amplifiers (SOAs) can be applied via a multi-pin connector at the housing. Metallic housing serves as mechanic protection for the photonic interior, and also eases the handling in the radiation pattern testbed.



### 3.2. Optical phased array

The terahertz wave  $E_{THz}$  generated by photomixing can be expressed as the envelope of the superposition of the two optical laser signals  $E_1$  and  $E_2$ . Each laser signal has the amplitude  $A_i$ , an angular frequency  $\omega_i = 2\pi f$ , and a phase  $\varphi_i$ :

$$E_i = A_i \cos(\omega_i t + \varphi_i). \quad (4)$$

Since the terahertz signal  $E_{THz}$  is proportional to the intensity of the optical beat signal, it is [2]

$$E_{THz} \propto E_{beat}^2 = |E_1 + E_2|^2 = |A_1 \cos(\omega_1 t + \varphi_1) + A_2 \cos(\omega_2 t + \varphi_2)|^2. \quad (5)$$

Assuming the same amplitude for the signals of the two lasers  $A_1 = A_2 = 1$ , it is

$$\begin{aligned} E_{beat}^2 &= |\cos(\omega_1 t + \varphi_1) + \cos(\omega_2 t + \varphi_2)|^2 \\ &= 1 + \frac{1}{2} \cos(2\omega_1 t + 2\varphi_1) + \frac{1}{2} \cos(2\omega_2 t + 2\varphi_2) \\ &\quad + \cos((\omega_1 + \omega_2)t + (\varphi_1 + \varphi_2)) + \cos((\omega_1 - \omega_2)t + (\varphi_1 - \varphi_2)). \end{aligned} \quad (6)$$

A constant offset and terms with frequency twice or the sum of the optical frequencies do not contribute to the terahertz signal. Hence, we can restrict to the difference frequency  $\Omega = \omega_1 - \omega_2$  to describe the optical beat signal, i.e., terahertz generation:

$$E_{THz} \propto \cos(\Omega t + \Phi). \quad (7)$$

The frequency of the terahertz signal is given by  $f_{THz} = \Omega/2\pi$ . The phase of the optical beat signal, i.e., the terahertz signal, is determined by the phase difference of the two optical signals  $\Phi = \varphi_1 - \varphi_2$ .

In order to set the phase difference  $\beta = \Phi_l - \Phi_{l+1}$  of neighboring optoelectronic antennas  $l$  (s.f. Figure 1), the phase of the optical signals must be manipulated individually. This can be realized by optical delay lines in free-space, a true time delay via an integrated Blass-matrix, or as an optical phased array using phase shifters [27,29,47–50]. Since our approach is an OPA based on phase shifters, the beam squint effect needs to be considered.

The beam squint effect describes the frequency-dependent beam angle of broadband signals. In a wireless communication scenario, the different frequency components of the data signal would be radiated toward different directions. In order to investigate the beam squint, i.e., the variation of the beam angle  $\Delta\theta^0$ , we take Eq. (1) and add a variation to the wavelength  $\lambda$  and phase difference  $\beta$ :

$$\cos(\theta^0 + \Delta\theta^0) = -\frac{\lambda + \Delta\lambda}{2\pi} \cdot \frac{\beta + \Delta\beta}{d}. \quad (8)$$

Hence, two causes for beam squint arise: i) the variation of the phase difference between neighboring antennas  $\Delta\beta$ , and ii) the variation of the radiated wavelength  $\Delta\lambda$ .

Based on the above mentioned equation, the phase difference can be expressed as

$$\Delta\beta = \Delta\Phi_l - \Delta\Phi_{l+1} = (\Delta\varphi_{1,l} - \Delta\varphi_{2,l}) - (\Delta\varphi_{1,l+1} - \Delta\varphi_{2,l+1}). \quad (9)$$

If we assume a fixed wavelength from the second optical laser signal, i.e., a fix phase contribution  $\Delta\varphi_2 = 0$ , Eq. (9) can be reduced to  $\Delta\beta \propto \Delta\varphi_{1,l} - \Delta\varphi_{1,l+1}$ . The optical phase at the end of the OPA is given by

$$\varphi_{1,l} = 2\pi \cdot \frac{n \cdot L_l}{\lambda_1} = L_l \cdot \omega_1 \cdot \frac{n}{c_0}. \quad (10)$$

In this equation,  $c_0$  is the speed of light and  $n$  is the constant refractive index. The path length  $L_l$  of the individual OPA channels are equal by design. Hence, the phase variation at the end of

each OPA channel depends only on the frequency variation, i.e., signal bandwidth:  $\Delta\varphi_{1,l} \propto \Delta\omega_1$  for all values of  $l$ . Considering equal phase variation at neighboring channels  $\Delta\varphi_{1,l} = \Delta\varphi_{1,l+1}$  for Eq. (9), the phase variation does not affect the phase of the beat signal, i.e., the terahertz signal:  $\Delta\beta = 0$  and  $\beta = \text{const.}$

The second potential cause for beam squint is the variation of the resulting radiated wavelength  $\Delta\lambda$ . To investigate the impact, the array factor is calculated as described in section 2.2 for the target wavelength  $\lambda$  and the wavelength variation  $\lambda \pm \Delta\lambda$ . In our case, the target frequency is 300 GHz and we assume up to 50 GHz signal bandwidth. For a phase shift of  $\beta = 45^\circ$ , the beam angle of the center frequency is  $\theta^0 = 60^\circ$ , whereas the frequency shifted signals are radiated at  $\theta_+^0 = 64.5^\circ$  and  $\theta_-^0 = 53.5^\circ$ , respectively. However, from the receiving perspective, the power penalty at the intended beam angle is the crucial figure of merit. At  $\theta = 60^\circ$ , the power penalty for signals at 300 GHz  $\pm$  50 GHz is less than 0.1 dB. This power variation can be easily compensated by pre-distortion at the transmitter. Thus, the beam squint effect can be neglected for this specific antenna array even for signal bandwidth as high as 50 GHz.

Note that the beam squint effect get more relevant for higher antenna gain, i.e., larger antenna array. If the power penalty increases, the OPA approach needs to be replaced by a Blass-matrix for example, what is still possible with our platform solution.

The OPA comprises a waveguide network which assures the correct phase difference and superposition of the optical signals for the respective photodiodes. In this waveguide network, multi-mode interferometers (MMIs) split and combine the optical signals. The required phase offset for each path is set statically through thermo-optical phase shifters (TOPSs) and is only changed when the beam angle is varied.

In this paper, we present an OPA based on the PolyBoard platform, which give some advantages compared to other material: Polymer materials show a fairly high thermo-optical coefficient of around  $-1.1 \times 10^{-4} K^{-1}$ , which is of the same order of magnitude than InP ( $2 \times 10^{-4} K^{-1}$ ) and Si ( $1.86 \times 10^{-4} K^{-1}$ ), and one order of magnitude larger than that of SiN ( $2.51 \times 10^{-5} K^{-1}$ ) [51–54]. Further, the thermal conductivity of polymer materials ( $0.29 W \cdot m^{-1} \cdot K^{-1}$ ) is two orders of magnitude lower than that of InP ( $68 W \cdot m^{-1} \cdot K^{-1}$ ) and SiN ( $30 W \cdot m^{-1} \cdot K^{-1}$ ), and three orders of magnitude lower than that of Si ( $156 W \cdot m^{-1} \cdot K^{-1}$ ) [53,55–57]. This makes polymers ideal candidates for highly efficient (i.e., low-power) thermo-optical phase shifters with low crosstalk due to the high heat confinements achievable. In addition, due to the low propagation loss of 0.8 dB/cm, the polymer waveguides are suitable for achieving the same optical path length for 4 channels with reasonable losses. On a more practical note, HHI's PolyBoard platform allows for passive fiber-to-chip coupling by means of U-grooves, which eases the miniaturization and packaging of such photonic phased array elements [58,59]. Furthermore, the PolyBoard platform can potentially enable the hybrid integration of phased arrays with other photonic functionalities such as tunable lasers and high-speed modulators, paving the way towards fully-photonic millimeter wave and terahertz emitters with high gain and beam steering capability [31].

The layout of the OPA is shown in Fig. 3(a). The two inputs consist of a U-groove for alignment-free coupling using fibers. Each input is connected to a  $1 \times 4$  MMI for power splitting, followed by an equidistant waveguide network to minimize the phase difference between different paths. Additionally, phase shifters are inserted in the waveguide network of the lower input to set the desired phase before superposition with the optical signal from the upper input. At the end of the network, the signals coming from the respective inputs, i.e., the different wavelength, are combined by means of  $1 \times 2$  MMIs. A  $1 \times 4$  fiber array is then followed and coupled to the output. In addition, the upper output channel includes a 10 dB tap coupler that directs a small portion of the beat signal to a  $45^\circ$  mirror at the upper edge of the chip. This allows the coupling of a fiber from the top to monitor the signal.

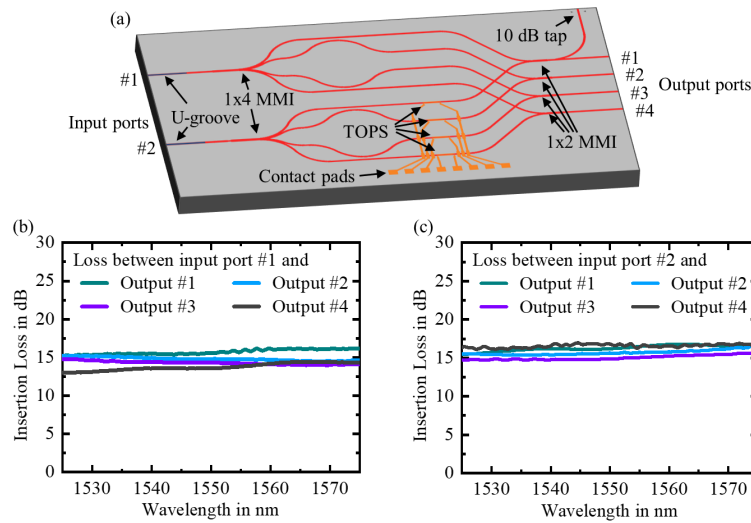


**Fig. 3.** (a) Layout of the OPA chip with two U-grooves for the fiber input and four cleaved facets at the output. Multi-mode interferometers (MMI) are used to split and combine the optical signals, respectively. Thermo-optical phase shifters (TOPS) allow to set the phase of the optical beat signal with current injection via the contact pads. For monitoring purposes, a 10 dB tap is included. The insertion loss between the respective input port and the four output ports is shown for the whole C-band in (b) and (c).

The devices were pre-characterized before performing the fiber assembly. Figure 3(a) shows the ports definition for inputs and outputs of the chip. Typical measured insertion losses for both inputs are shown in Fig. 3(b) and (c). As can be seen, the losses show a fairly wavelength-independent behavior within the optical C-band. Theoretically, due to the  $1 \times 4$  and  $1 \times 2$  MMI in the waveguide network 9 dB losses are introduced into each path. From the 6 dB of excess loss, 1.1 dB can be attributed to propagation in the waveguide considering 0.8 dB/cm propagation loss, 1.2 dB to the coupling losses of the cleaved fibers inserted in the U-groove, and 1.0 dB to suboptimal coupling of the fibers coupled at the output ports. The remaining 2.8 dB losses may be attributed to non-ideal behavior of the other photonic building blocks implemented on the PolyBoard OPA. The different losses at the respective output ports are mainly attributed to not completely balanced MMIs.

Figure 4(a) shows the photonic assembly of the OPA including the polymer chip, optical fibers at input and output, and an electronic plug to drive the phase shifters. The optical input signals are fed into the polymer chip by two individual optical fibers from the left side, which are aligned to the polymer waveguides using U-grooves in the polymer. The four output channels are coupled to an array of four optical fibers with a pitch of 250  $\mu\text{m}$ . The array is aligned actively in front of the polymer waveguides and then fixed with optical epoxy. Spot size converters in polymer assure the matching of the mode field diameter between fiber and chip. In order to drive the phase shifting network in the beam steering testbed, the OPA is connected by wire bonding with a multi-pin socket. The micrograph of the polymer chip in Fig. 4(b) reveals the U-grooves at the left edge of the chip and the TOPSs with gold plated bias lines. The optical waveguides including the MMIs appear as bright lines.



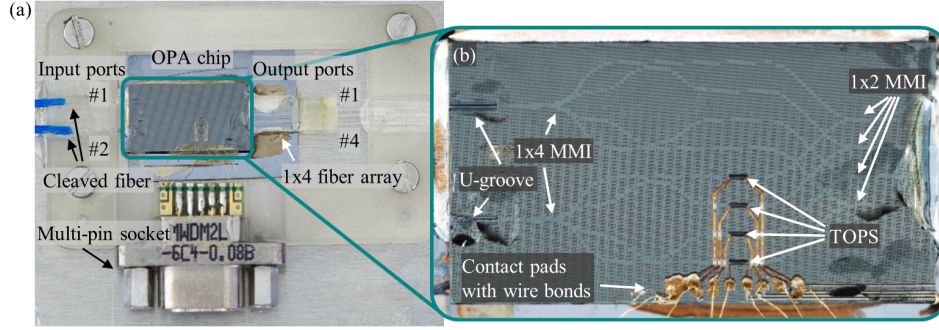


**Fig. 4.** (a) Photograph of the assembled OPA chip with two individual optical fibers on the left side plugged into U-grooves of the polymer chip. The 4 output channels are coupled to a fiber array with 250  $\mu\text{m}$  pitch. Wire bonding to a multi-pin plug allows stable connection and driving of the OPA in the beam steering testbed. The augmented micrograph (b) shows the polymer-based OPA chip with 4 thermo-optical phase shifters (TOPS) to set the phased of the beat signal at the respective output port.

## 4. Characterization and beam steering

### 4.1. Characterization of the optical phased array

In order to control the beam steering of the emitter array, the thermo-optical phase shifters of the OPA need to be characterized. To measure the phase shift of an optical signal introduced by a TOPS, a fiber-based Mach-Zehnder interferometer (MZI) is arranged. Figure 5(a) shows the schematic experimental setup. A single mode laser (APEX AP3350A) with emission in the C-band is connected to the fiber of input #2 of the packaged OPA. The  $1 \times 4$  MMI splits the input signal to the four channels of the OPA, which pass the TOPSs. Hence, the particular phase of the optical signals at the four output fibers depends on the applied current of the respective TOPS. Two of the output fibers are combined with a 3-dB fiber coupler and then fed to a power meter (Thorlabs PM100D). The measured power will be maximized when the two OPA output signals interfere with same phase and minimized when the phase is shifted by  $\pi$ . A multi-channel current controller (Thorlabs Pro8000) injects the required current to the phase shifters. Both devices are connected to a computer (PC) that runs automated measurements of power meter as a function of the current at each phase shifter. Note that the MZI consists of two arms with approx. 2 m optical fiber length each, which makes it very sensitive to movement of the fibers or temperature change that translates to changes of the path length. Thus, automated, i.e., fast, measurements are required to acquire reliable data. Therefore, the current controller addresses 60 values between 0 mA and 20 mA in less than 1 minute. Within this duration, we could observe a stable MZI behavior.

The following relationship between the normalized optical power  $P_n$  and heating power of a phase shifter  $P_{PS}$  is derived:

$$P_n = \cos \left( \frac{P_{PS}}{P_\pi} \pi + \frac{P_{MZI}}{P_\pi} \pi \right). \quad (11)$$

Here  $P_n$  denotes the electrical heating power required for a phase shift of  $\beta = \pi$ , and  $P_{MZI}$  is a static offset for the respective channel of the MZI, which is caused by path length differences. Assuming a constant electrical resistance of the phase shifter  $R_{PS}$ , the above equation can be rewritten as follows:

$$P_n = \cos \left( \frac{I_{PS}^2 R_{PS}}{I_\pi^2 R_{PS}} \pi + \frac{I_{MZI}^2 R_{PS}}{I_\pi^2 R_{PS}} \pi \right) = \cos \left( \frac{I_{PS}^2 + I_{MZI}^2}{I_\pi^2} \pi \right), \quad (12)$$

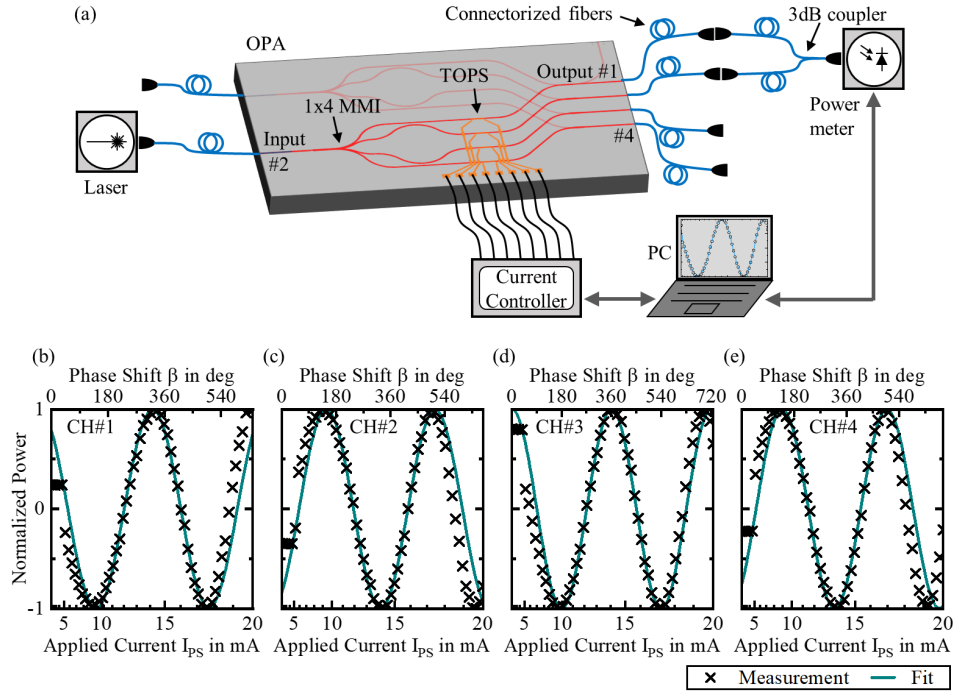


**Fig. 5.** (a) Arrangement for a fiber-based Mach-Zehnder interferometer (MZI) to characterize the thermo-optical phase shifter (TOPS) of the OPA. A single mode laser is connected to the input port #2 that passes the light to the four TOPSs. A 3-dB fiber coupler combines two of the OPA channels and feeds the optical power meter. A current controller drives the individual TOPSs. A computer (PC) controls current controller and acquires data. (b) – (e) show the measured signal of the power meter as a function of the applied current at the TOPS ( $I_{PS}$ ) (black crosses). The correlation between applied current and resulting phase shift is extracted by a fitting function (green line). Based on the fitting results, the upper x-scale indicates the introduced phase shift  $\beta$ .

where  $\sqrt{I_{PS}^2 + I_{MZI}^2}$  is the current applied at the heating element of the phase shifter.  $I_{\pi}$  is the current that is required for a phase shift of  $\beta = \pi$ .  $I_{MZI}$  is an offset current, which only applies due to path length differences in the fiber-based MZI. This offset is only relevant to model the MZI measurements. Thus, the actual phase shift is given by:

$$\beta = \frac{I_{PS}^2}{I_{\pi}^2} \pi. \quad (13)$$

Figure 5(b) to (e) show the results of the OPA characterization of the individual channels. The black crosses denote the measured optical signal as a function of the current of the respective phase shifter. The green lines are the phase shift modeled with the above formulas and fitted to the measured data. Based on these fits, we determine the required current for a phase shift of  $\beta = \pi$  of the four OPA channels to be:  $I_{\pi} = 10.6$  mA for channel#1,  $I_{\pi} = 10.4$  mA for channel#2,  $I_{\pi} = 9.95$  mA for channel#3, and  $I_{\pi} = 10.2$  mA for channel#4. As the resistance of the phase shifters is  $R_{PS} = 15.2 \Omega$ , the average required power for a  $\pi$  phase shift is as low as  $P_{\pi} = 1.6$  mW. Note that the thermo-optic phase shifters operate in a linear regime for  $I_{PS} > 10$  mA only. Thus, this offset will be applied to each TOPS for the following measurements.

We investigated the thermal crosstalk behavior between channels measuring the optical signal while tuning neighboring phase shifters. Due to the low thermal conductivity of the polymer material ( $0.29 \text{ W} \cdot \text{m}^{-1} \cdot \text{K}^{-1}$ ), we did not observe a notable change of the optical signal. Therefore, thermal crosstalk can be neglected for operation of the OPA.

#### 4.2. Radiation pattern and beam steering

After characterizing the OPA, beam steering can be demonstrated using the  $1 \times 4$  emitter array. The experimental setup is schematically shown in Fig. 6(a). Two single mode lasers (APEX AP3350A) are connected to the fiber-coupled OPA module. The lasers operate in the optical C-band, whereas the frequency spacing of them is 300 GHz, i.e., the target frequency for our beam steering scenario. Thanks to the waveguide network of the OPA chip, each of the output fibers provides a 300 GHz optical beat signal. The phase of each beat signal is manipulated by the current  $I_{\text{PS}}$  at the respective phase shifter, which is set using a current controller (Thorlabs Pro8000). Erbium-doped fiber amplifiers (EDFAs, Thorlabs EDFA100P) compensate the losses of the OPA module (s.f.3.2) before the optical signal is fed into the fiber-pigtailed emitter module (Tx). The SOA currents are set in a way that the resulting photocurrent of each PD of the array is 1 mA. The bias voltage of the PDs is applied by a waveform generator (Keithley 3390) as a 20 kHz square wave from  $-1 \text{ V}$  to  $0 \text{ V}$ . The antenna array is mounted on an automated rotation stage in order to change the angle toward the detector (Rx). The detector, i.e., a Schottky barrier diode (SBD) with silicon lens (ACST A1), is placed 20 cm in front of the emitter. Due to the square wave biasing, i.e., on-off-modulation of the terahertz signal, the detector output signal can be acquired by a lock-in amplifier (LIA, Signal Recovery 7265), which is synchronized with the bias source. A computer (PC) orchestrates current controller, rotation stage, and LIA in order to acquire the radiation pattern of the antenna array from  $0^\circ$  to  $180^\circ$  as a function of the phase shift  $\beta$ . The photograph on the right in Fig. 6(a) shows the emitter on the rotation stage (left) and the receiver on the right.

Figure 6(b) shows the measured H-plane (black) and E-plane (blue) of a single antenna element (AE). The lens shaped surface of the hyper-hemicylindrical silicon lens results in a pencil beam in the E-plane with a 3-dB width of less than  $5^\circ$ . Since beam steering only takes place in the H-plane, a highly directional E-plane is desirable in order to target the detector. The H-plane of an AE features a broader radiation pattern. The 3-dB width measures approx.  $31^\circ$ , which allows an interplay of the four AE for beam steering in the H-plane. Figure 6(c) shows the AF (red dashed line) of the array of four antennas in case all antennas are driven with the same phase, i.e.,  $\beta = 0^\circ$ . For this setting, the beam angle of the AF is  $\theta_{\text{AF}}^0 = 90^\circ$  and, thus, coincides with the main lobe of a single bowtie antenna. However, the AF increases the directivity of the array emitter compared to a single AE. The resulting radiation pattern of the array can be predicted by multiplication of measured AE and calculated AF (green line). In case of a phase difference at the antenna elements of  $\beta = 35^\circ$  (Fig. 6(d)), the AF predicts a beam angle of  $\theta_{\text{AF}}^0 = 113^\circ$ . Due to the anisotropic H-plane of the AE, the actual maximum of the predicted radiation pattern (green line) is not at  $113^\circ$ . Thus, in order to rate the actual radiation pattern, we introduce the effective beam angle  $\theta_e^0$ , which is defined as the center between the angles at which the power of the main lobe dropped by 3 dB, i.e., the center of the 3-dB lobe. In case of  $\beta = 35^\circ$  the predicted effective beam angle (green dashed arrow) of our array is  $\theta_e^0 = 99^\circ$ . Note that all radiation patterns of Fig. 6 are normalized in order to illustrate the differences between AE and the predicted pattern due to the AF. However, due to the superposition of the electric field of the four antennas, actually 12 dB higher power can be expected from the array compared to the single AE.

According to these theoretical considerations based on AF and AE, the measured radiation patterns of the emitter array can be analyzed. The radiation patterns for six different phase settings between  $-60^\circ$  and  $+60^\circ$  are depicted in Fig. 7. The calculated radiation patterns (black dashed lines) agree very well with the measured patterns (green solid lines). Note that the

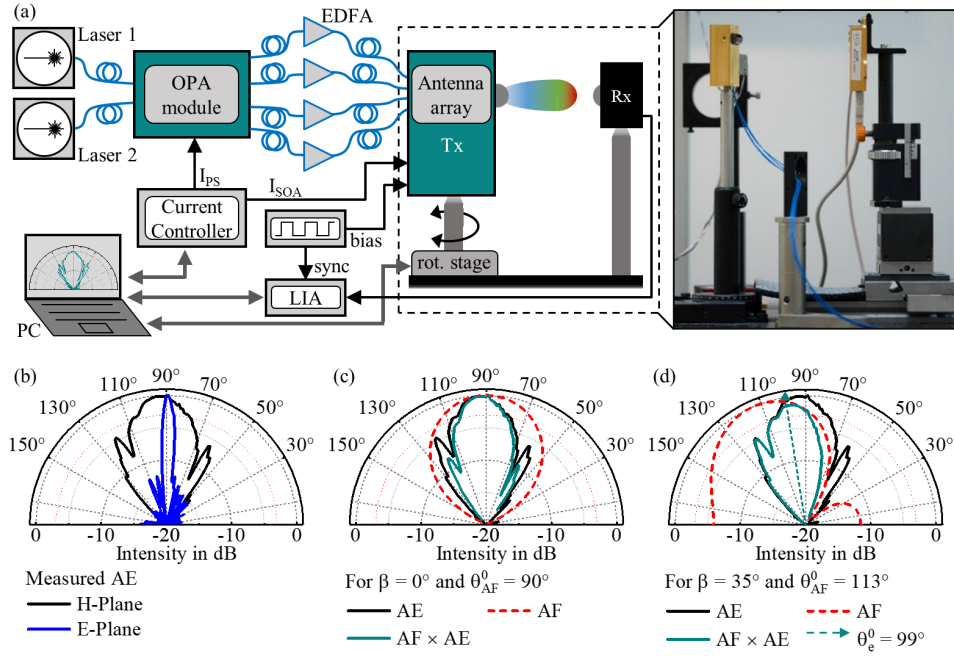


**Fig. 6.** (a) Setup for measurements of the radiation pattern: Two lasers are connected to the OPA's input ports. EDFAs between OPA and emitter (Tx) compensate the coupling losses. The antenna array converts the optical signal into a terahertz signal. The bias of the PDs is applied as a square wave voltage. A commercial Schottky barrier diode is used as receiver (Rx) in 20 cm distance. The rotation stage, which mounts the Tx, allows to vary the angle between Tx and Rx. A lock-in amplifier (LIA) recovers the detector signal. A computer (PC) controls the beam steering and acquires the detected signal as a function of the angle. The photograph shows the Tx module on the rotation stage (left) and the Rx (right). (b) shows the measured radiation pattern in the E-plane (blue) and H-plane (black) for a single antenna. (c) The expected H-plane radiation of the  $1 \times 4$  array ( $\beta = 0^\circ$ ) is the product of the measured single antenna element AE (black line) and the array factor (AF) (dashed red line). (d) For a phase shift of  $\beta = 35^\circ$ , the AF predicts a beam angle of  $\theta_{AF}^0 = 113^\circ$ . The product of AF and AE indicates an effective beam angle of  $\theta_e^0 = 99^\circ$  (green arrow).

agreement between measurement and calculation also confirms that there is no thermal crosstalk between the phase shifters. The effective beam angle  $\theta_e^0$  is indicated by the dashed green arrow as in Fig. 6(d). For comparison, the beam profile of the single emitter is included as a gray line in each partial figure.

For the phase shift of  $\beta = \pm 20^\circ$  in Fig. 7(a) and (d), the AF suggest a scan sector of  $\Delta\theta_{AF}^0 = 26^\circ$ , i.e., from  $\theta_{AF}^0 = 77^\circ$  to  $\theta_{AF}^0 = 103^\circ$  beam angle. Due to the anisotropic radiation of the single antenna element, however, the effective beam angle is only  $\theta_e^0 = 88^\circ$  and  $\theta_e^0 = 96^\circ$ . Consequently the effective scan sector is  $\Delta\theta_e^0 = 8^\circ$ . For a phase shift of  $\beta = \pm 40^\circ$  (Fig. 7(b) and (e)), the AF features a scan sector of  $\Delta\theta_{AF}^0 = 52^\circ$ . Here the effective beam steering range is  $\Delta\theta_e^0 = 14^\circ$ . An effective scan sector of  $\Delta\theta_e^0 = 20^\circ$  are measured for a phase shift of  $\beta = \pm 60^\circ$  (Fig. 7(c) and (f)), whereas the AF would allow for  $\Delta\theta_{AF}^0 = 84^\circ$ .

The intensity of the main lobe decreases for increasing beam angles, just as the intensity of the radiation of an anisotropic single emitter decreases. Nevertheless, the power level of the tilted beam (s.f. (c) and (f)) is still more than 6 dB higher than the power of the single emitter. Note

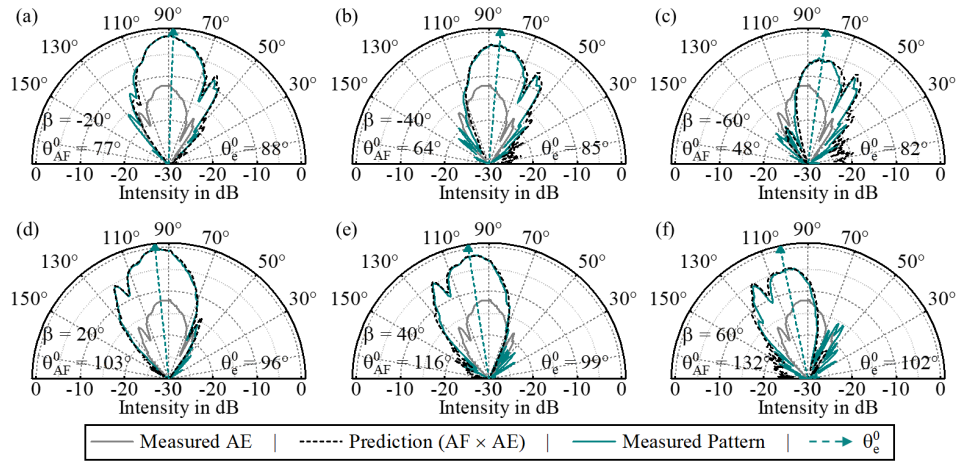


**Fig. 7.** Measured radiation for different phase differences  $\beta$  and the corresponding modeled radiation resulting from the array factor and the radiation of the single emitter. Radiation from a single emitter is shown for reference. The superposition of the E-fields in the  $1 \times 4$  array results in a 12 dB difference between the single emitter and the array of 4.

that the side lobe of the initial radiation pattern is fed when the steering angle is beyond the lobe. However, in our measurements, most of the power is still contained in the main lobe for all beam angles.

## 5. Conclusion

In this paper, we investigated the beam steering capability of a phased array of optoelectronic antennas at 300 GHz. The linear emitter array consists of four indium phosphide (InP) based photodiodes (PDs) with bowtie antennas, which were mounted on a hyper-hemicylindrical silicon lens. The antenna array was fabricated using the generic InP foundry platform at Fraunhofer HHI. The fiber-pigtailed emitter array was orchestrated by an optical phased array (OPA) based on polymer waveguides, which was realized using the PolyBoard platform at Fraunhofer HHI. In order to set the phase of the individual antennas, thermo-optic phase shifters are integrated on the polymer waveguides. Thus, the optical feed signal for the PDs was controlled while the radiation pattern of the emitter was measured for various phase setting. For straight radiation, we observed 10.6 dB higher power from the  $1 \times 4$  array than from the single emitter, which is close to the theoretical 12 dB gain of an array of four elements. The 3-dB width of a single emitter is  $31^\circ$ , whereas the array reduces the 3-dB width to  $22.5^\circ$ . Thus, two objectives of antenna arrays are successfully achieved: increased output power and higher directivity. In addition, a continuous beam steering across  $20^\circ$  was demonstrated when the phase difference of neighboring antennas was swept between  $-60^\circ$  to  $60^\circ$ . Modeled and measured radiation pattern agree very well for all phase settings, which confirms the proper design of the antenna array. Moreover, we predicted and confirmed the impact of the silicon lens to the beam angle and width of the beam lobe according to Snell's law. Thus, we experimentally demonstrated that (i) waveguide-integrated phase shifters in the optical domain can be used for a phased array, and (ii) in combination with a  $1 \times 4$  photonic emitter array continuous steering of a terahertz beam at 300 GHz is enabled. This is the first demonstration of a phased array antenna in the terahertz frequency band using a polymer-based OPA and an InP-based emitter array.

A high directivity and the ability to dynamically point towards different receiver locations is especially important for point-to-point and point-to-multipoint communication within B5G



scenarios. In this regard, the present work is an important step towards photonic-enabled wireless communication in the terahertz band. Based on the presented results, three major challenges need to be addressed for future photonic communication systems: First, the realization of a 2-dimensional array in order to enable beam steering in two dimensions. Second, a higher level of photonic integration, including lasers and modulators, for compact and robust transceiver units. Third, overcoming the low coupling efficiency from substrate to air. Regarding the first and second challenge, waveguide-integrated photonic platforms are a key-enabler to feed PDs in a 2-dimensional arrangement with sufficient optical power. Regarding the third objective, we successfully used a hyper-hemicylindrical substrate lens for the 1-dimensional array. However, this approach is not suitable for 2-dimensional arrays. In addition, a substrate lens limits the directivity and steering capability due to internal reflection. Therefore, other concepts for coupling from substrate into air, or directly from the antennas into air need to be explored in future work.

In general, we did not identify any fundamental limitation for the photonic approach and the mentioned objectives are addressed in our ongoing project. Therefore, we conclude that photonic integrated antenna arrays promise to be a scalable and flexible solution for future wireless communications. In addition, hybrid integration offers great potential for future applications by facilitating the combination of different waveguide-coupled photonic platforms. This will allow to exploit the individual functional components for complex millimeter wave and terahertz transceivers, in the future.

**Funding.** H2020 LEIT Information and Communication Technologies (871668); Bundesministerium für Bildung und Forschung (16KIS0638).

**Acknowledgment.** This work was supported by TERAway project that has received funding from the European Union's Horizon 2020 Research and Innovation Programme under G.A No 871668 and it is an initiative of the Photonics Public Private Partnership.

This work was funded by Bundesministerium für Bildung und Forschung (BMBF) in the project PHONOGRAPH (16KIS0638).

**Disclosures.** The authors declare no conflicts of interest.

**Data availability.** Data underlying the results presented in this paper are not publicly available at this time but may be obtained from the authors upon reasonable request.

## References

1. M. Deumer, S. Breuer, R. Kohlhaas, S. Nellen, L. Liebermeister, S. Lauck, M. Schell, and B. Globisch, "Continuous wave terahertz receivers with 4 . 5 THz bandwidth and 112 dB dynamic range," *Opt. Express* **29**(25), 41819–41826 (2021).
2. S. Preu, G. H. Döhler, S. Malzer, L. J. Wang, and A. C. Gossard, "Tunable, continuous-wave terahertz photomixer sources and applications," *J. Appl. Phys.* **109**(6), 061301 (2011).
3. M. Naftaly, N. Vieweg, and A. Deninger, "Industrial applications of terahertz sensing: State of play," *Sensors* **19**(19), 4203 (2019).
4. L. Liebermeister, S. Nellen, R. B. Kohlhaas, S. Lauck, M. Deumer, S. Breuer, M. Schell, and B. Globisch, "Optoelectronic frequency-modulated continuous-wave terahertz spectroscopy with 4 THz bandwidth," *Nat. Commun.* **12**(1), 1071 (2021).
5. D. M. Mittleman, "Twenty years of terahertz imaging [invited]," *Opt. Express* **26**(8), 9417–9431 (2018).
6. IEEE, "IEEE Standard for High Data Rate Wireless Multi-Media Networks—Amendment 2: 100 Gb/s Wireless Switched Point-to-Point Physical Layer," IEEE Std 802.15.3d-2017 (Amendment to IEEE Std 802.15.3-2016 as Amend. by IEEE Std 802.15.3e-2017) 2017, 1–55 (2017).
7. J. F. Federici, J. Ma, and L. Moeller, "Review of weather impact on outdoor terahertz wireless communication links," *Nano Commun. Netw.* **10**, 13–26 (2016).
8. T. Nagatsuma and G. Carpintero, "Recent progress and future prospect of photonics-enabled terahertz communications research," *IEICE Trans. Electron.* **E98.C**(12), 1060–1070 (2015).
9. G. Ducournau, P. Szriftgiser, F. Pavanello, E. Peytavit, M. Zaknoute, D. Bacquet, A. Beck, T. Akalin, J. F. Lampin, and J. F. Lampin, "THz communications using photonics and electronic devices: the race to data-rate," *J. Infrared, Millimeter, Terahertz Waves* **36**(2), 198–220 (2015).
10. T. Kürner, D. M. Mittleman, and T. Nagatsuma, "Introduction to THz Communications," *Springer Ser. Opt. Sci.* **234**, 1–12 (2022).

11. T. Kürner, V. Petrov, and I. Hosako, "Standards for THz Communications," *Springer Ser. Opt. Sci.* **234**, 503–514 (2022).
12. T. Nagatsuma, G. Ducournau, and C. C. Renaud, "Advances in terahertz communications accelerated by photonics," *Nat. Photonics* **10**(6), 371–379 (2016).
13. A. J. Seeds, H. Shams, M. J. Fice, and C. C. Renaud, "TeraHertz photonics for wireless communications," *J. Lightwave Technol.* **33**(3), 579–587 (2015).
14. I. Dan, P. Szriftgiser, E. Peytavit, J. F. Lampin, M. Zegaoui, M. Zaknoute, G. Ducournau, and I. Kallfass, "300 GHz Wireless Link Employing a Photonic Transmitter and Active Electronic Receiver with a Transmission Bandwidth of 54 GHz," *IEEE Trans. Terahertz Sci. Technol. (c)*, 1–11 (2020).
15. T. Harter, S. Ummethala, M. Blaicher, S. Muehlbrandt, S. Wolf, M. Weber, M. M. H. Adib, J. N. Kemal, M. Merboldt, F. Boes, S. Nellen, A. Tessmann, M. Walther, B. Globisch, T. Zwick, W. Freude, S. Randel, and C. Koos, "Wireless THz link with optoelectronic transmitter and receiver," *Optica* **6**(8), 1063 (2019).
16. C. Castro, S. Nellen, R. Elschner, I. Sackey, R. Emmerich, T. Merkle, B. Globisch, D. De Felipe, and C. Schubert, "32 Gbd 16QAM Wireless Transmission in the 300 GHz Band using a PIN Diode for THz Upconversion," in *Optical Fiber Communications Conference and Exhibition* (2019), paper M4F.5.
17. S. Jia, L. Zhang, S. Wang, W. Li, M. Qiao, Z. Lu, N. M. Idrees, X. Pang, H. Hu, X. Zhang, L. K. Oxenlowe, and X. Yu, " $2 \times 300$  Gbit/s Line Rate PS-64QAM-OFDM THz Photonic-Wireless Transmission," *J. Lightwave Technol.* **38**(17), 4715–4721 (2020).
18. S. Nellen, S. Lauck, E. Peytavit, P. Szriftgiser, M. Schell, G. Ducournau, and B. Globisch, "Coherent Wireless Link at 300 GHz with 160 Gbit/s Enabled by a Photonic Transmitter," *J. Lightwave Technol.* **40**(13), 4178–4185 (2022).
19. T. Li, L. Gonzalez-Guerrero, H. Shams, C. Renaud, A. J. Seeds, M. Fice, I. White, and R. Pentty, "Novel compressed digital radio fronthaul over photonically-generated THz wireless bridge," in *Optical Fiber Communication Conference* (2020), Part F174-, pp. 2–4.
20. S.-R. Moon, S. Han, S. Yoo, H. Park, W.-K. Lee, J. K. Lee, J. Park, K. Yu, S.-H. Cho, and J. Kim, "Demonstration of photonics-aided terahertz wireless transmission system with using silicon photonics circuit," *Opt. Express* **28**(16), 23397–23408 (2020).
21. A. Morales, G. Nazarikov, S. Rommel, C. Okonkwo, and I. Tafur Monroy, "Highly Tunable Heterodyne Sub-THz Wireless Link Entirely Based on Optoelectronics," *IEEE Trans. Terahertz Sci. Technol.* **11**(3), 261–268 (2021).
22. T. Nagatsuma and G. Ducournau, "Photonics-Based Transmitters and Receivers," *Springer Ser. Opt. Sci.* **234**, 299–314 (2022).
23. S. Nellen, S. Lauck, G. Schwanke, M. Deumer, R. B. Kohlhaas, L. Liebermeister, M. Schell, and B. Globisch, "Radiation pattern of planar optoelectronic antennas for broadband continuous-wave terahertz emission," *Opt. Express* **29**(6), 8244 (2021).
24. J. Smith, M. Naftaly, S. Nellen, and B. Globisch, "Beam profile characterisation of an optoelectronic silicon lens-integrated pin-pd emitter between 100 ghz and 1 thz," *Appl. Sci.* **11**(2), 465 (2021).
25. C. A. Balanis, "Arrays: Linear, Planar, and Circular," in *Antenna Theory: Analysis and Design*, 4th ed. (John Wiley & Sons Inc., 2016), pp. 285–329.
26. M. Ali, A. Rivera-Lavado, Á. J. Pascual-Garcia, D. González-Ovejero, R. Sauleau, L. E. García-Muñoz, and G. Carpintero, "Antenna Arrays for Beamforming," *Springer Ser. Opt. Sci.* **234**, 161–174 (2022).
27. H. Kanaya, K. Tsugami, G. Sakano, G. C. Eu, and K. Kato, "Development of  $4 \times 4$  phased array antenna on chip for 300 GHz band application," in *SPIE OPTO* (2018), 1053114(February), p. 40.
28. M. Ali, R. Cruzoe-Guzman, L. E. Garcia-Munoz, F. Van Dijk, and G. Carpintero, "Photonics-enabled Millimetre-wave Phased-Array Antenna with True Time Delay Beam-steering," *2020 50th Eur. Microw. Conf.*, 316–319 (2021).
29. M. Che, Y. Matsuo, H. Kanaya, H. Ito, T. Ishibashi, and K. Kato, "Optoelectronic THz-Wave Beam Steering by Arrayed Photomixers With Integrated Antennas," *IEEE Photonics Technol. Lett.* **32**(16), 979–982 (2020).
30. G. Carpintero, K. Balakier, Z. Yang, R. C. Guzmán, A. Corradi, A. Jimenez, G. Kervella, M. J. Fice, M. Lamponi, M. Chitoui, F. Van Dijk, C. C. Renaud, A. Wonfor, E. A. J. M. Bente, R. V. Pentty, I. H. White, and A. J. Seeds, "Microwave photonic integrated circuits for millimeter-wave wireless communications," *J. Lightwave Technol.* **32**(20), 3495–3501 (2014).
31. T. Qian, M. Deumer, Y. D. Gupta, S. Nellen, B. Schuler, H. Conradi, M. Kresse, J. Reck, K. Mihov, M. Kleinert, M. Weigel, C. Zawadzki, D. De Felipe, B. Globisch, M. Baier, N. Keil, and M. Schell, "Hybrid Polymer THz Receiver PIC with Waveguide Integrated Photoconductive Antenna: Concept and 1st Characterization Results," *Opt. Fiber Commun. Conf. Exhib.* 24–26 (2022).
32. "IEEE Standard Definitions of Terms for Antennas," IEEE Std 145-2013 (Revision IEEE Std 145-1993) 1–50 (2014).
33. S. Nellen, T. Ishibashi, A. Deninger, R. B. Kohlhaas, L. Liebermeister, M. Schell, and B. Globisch, "Experimental Comparison of UTC- and PIN-Photodiodes for Continuous-Wave Terahertz Generation," *J. Infrared, Millimeter, Terahertz Waves* **41**(4), 343–354 (2020).
34. P.-K. Lu and M. Jarrahi, "Plasmonics-enhanced Photoconductive Terahertz Devices," *Fundam. Terahertz Devices Appl.* 187–219 (2021).
35. M. Bauer, A. Rämmer, S. A. Chevtchenko, K. Y. Osipov, D. Cibraite, S. Pralgauskaite, K. Ikamas, A. Lisauskas, W. Heinrich, V. Krozer, and H. G. Roskos, "A High-Sensitivity AlGaIn/GaN HEMT Terahertz Detector with Integrated Broadband Bow-Tie Antenna," *IEEE Trans. Terahertz Sci. Technol.* **9**(4), 430–444 (2019).

36. T. Ishibashi, Y. Muramoto, T. Yoshimatsu, and H. Ito, "Unitraveling-Carrier Photodiodes for Terahertz Applications," *IEEE J. Sel. Top. Quantum Electron.* **20**(6), 79–88 (2014).
37. J. P. Seddon, M. Natrella, X. Lin, C. Graham, C. C. Renaud, and A. J. Seeds, "Photodiodes for terahertz applications," *IEEE J. Sel. Top. Quantum Electron.* **28**(2: Optical Detectors), 1–12 (2022).
38. D. F. Filipovic, S. S. Gearhart, and G. M. Rebeiz, "Double-Slot Antennas on Extended Hemispherical and Elliptical Silicon Dielectric Lenses," *IEEE Trans. Microw. Theory Tech.* **41**(10), 1738–1749 (1993).
39. T. H. Büttgenbach, "An Improved Solution for Integrated Array Optics in Quasi-Optical mm and Submm Receivers: The Hybrid Antenna," *IEEE Trans. Microw. Theory Tech.* **41**(10), 1750–1760 (1993).
40. J. Van Rudd and D. M. Mittleman, "Influence of substrate-lens design in terahertz time-domain spectroscopy," *J. Opt. Soc. Am. B* **19**(2), 319–329 (2002).
41. C. C. Renaud, M. Natrella, C. Graham, J. Seddon, F. Van Dijk, and A. J. Seeds, "Antenna integrated THz uni-traveling carrier photodiodes," *IEEE J. Sel. Top. Quantum Electron.* **24**(2), 1–11 (2018).
42. V. H. Rumsey, "Frequency independent antennas," in *IRE International Convention Record* (Institute of Electrical and Electronics Engineers, 1966), 5, pp. 114–118.
43. K. Kolpatzeck, X. Liu, B. Friederich, D. Damyanov, L. Haring, T. Schultze, J. C. Balzer, and A. Czyliw, "Wideband Radiation Pattern Measurement of Terahertz Antenna-Integrated Photodiodes by Frequency-Domain Spectroscopy," 1–5 (2019).
44. R. C. Comton, R. C. McPhedran, Z. Popovic, G. M. Rebeiz, P. P. Tong, and D. B. Rutledge, "Bow-Tie Antennas on a Dielectric Half-space : Theory and Experiment," *IEEE Trans. Antennas Propag.* **AP 35**(6), 622–631 (1987).
45. N. Grote, M. Baier, and F. Soares, "Photonic Integrated Circuits on InP," in *Springer Series in Optical Sciences* (Springer, 2017), 161, pp. 799–840.
46. F. M. Soares, M. Baier, T. Gaertner, N. Grote, M. Moehrl, T. Beckerwerth, P. Runge, and M. Schell, "InP-based foundry PICs for optical interconnects," *Appl. Sci.* **9**(8), 1588 (2019).
47. M. Che, Y. Matsuo, K. Kondo, and K. Kato, "Arrayed uni-traveling-carrier photodiodes for pulsed THz wave beam steering," *Int. Top. Meet. Microw. Photonics*, 9–12 (2021).
48. C. Tsokos, E. Andrianopoulos, A. Raptakis, N. Lyras, L. Gounaridis, P. Groumas, R. B. Timens, I. Visscher, R. Grootjans, L. S. Wefers, D. Geskus, E. Klein, H. Avramopoulos, R. Heideman, C. Kouloumentas, and C. Roeloffzen, "True Time Delay Optical Beamforming Network Based on Hybrid Inp-Silicon Nitride Integration," *J. Lightwave Technol.* **39**(18), 5845–5854 (2021).
49. C. Tsokos, E. Mylonas, P. Groumas, V. Katopodis, L. Gounaridis, R. B. Timens, R. M. Oldenbeuving, C. G. H. Roeloffzen, H. Avramopoulos, and C. Kouloumentas, "Analysis of a Multibeam Optical Beamforming Network Based on Blass Matrix Architecture," *J. Lightwave Technol.* **36**(16), 3354–3372 (2018).
50. B. Paul, K. Sertel, and N. K. Nahar, "Photonic Beamforming for 5 G and Beyond: A Review of True Time Delay Devices Enabling Ultra-Wideband Beamforming for mmWave Communications," *IEEE Access* **10**(May), 75513–75526 (2022).
51. ChemOptics Inc., "Singlemode Waveguide Resin," <http://www.chemoptics.co.kr/en/sub/products/materials/LFR.php>.
52. G. Cocorullo, F. G. Della Corte, and I. Rendina, "Temperature dependence of the thermo-optic coefficient in crystalline silicon between room temperature and 550 K at the wavelength of 1523 nm," *Appl. Phys. Lett.* **74**(22), 3338–3340 (1999).
53. S. A. Clark, B. Culshaw, E. J. Dawney, and I. E. Day, "Thermo-optic phase modulators in SIMOX material," in *Integrated Optics Devices IV* (2000), 3936(March 2000), pp. 16–24.
54. A. W. Elshaari, I. E. Zadeh, K. D. Jöns, and V. Zwiller, "Thermo-Optic Characterization of Silicon Nitride Resonators for Cryogenic Photonic Circuits," *IEEE Photonics J.* **8**(3), 1–9 (2016).
55. M. M. Rahman and M. F. Hossain, "Thermal performance analysis of polymer optical waveguides for thermo-optic applications," 2014 9th Int. Forum Strateg. Technol. IFOST 2014 65–68 (2014).
56. M. Takenaka and S. Takagi, "InP-based photonic integrated circuit platform on SiC wafer," *Opt. Express* **25**(24), 29993 (2017).
57. K. Hirao, K. Watari, M. E. Brito, M. Toriyama, and S. Kanzak, "Journal of the American Ceramic Society - September 1996 - Hirao - High Thermal Conductivity in Silicon Nitride with.pdf," *J. Am. Ceram. Soc.* **79**(9), 2485–2488 (1996).
58. Z. Zhang, D. Felipe, and V. Katopodis, *et al.*, "Hybrid photonic integration on a polymer platform," *Photonics* **2**(3), 1005–1026 (2015).
59. M. Kleinert, D. de Felipe, C. Zawadzki, W. Brinker, J. H. Choi, P. Reinke, M. Happach, S. Nellen, M. Möhrle, H.-G. Bach, N. Keil, and M. Schell, "Photonic integrated devices and functions on hybrid polymer platform," in *SPIE OPTO* (2017), 10098, p. 100981A.